

Coupled urban wind flow and indoor natural ventilation modelling on a high-resolution grid: A case study for the Amsterdam ArenA stadium

T. van Hooff ^{(a,b),1,*}, B. Blocken ^(a)

(a) Building Physics and Systems, Eindhoven University of Technology, P.O. box 513, 5600 MB Eindhoven, The Netherlands

(b) Laboratory of Building Physics, Katholieke Universiteit Leuven, Kasteelpark Arenberg 40, 3001 Leuven, Belgium

ABSTRACT

Wind flow in urban environments is an important factor governing the dispersion of heat and pollutants from streets, squares and buildings. This paper presents a coupled CFD modelling approach for urban wind flow and indoor natural ventilation. A specific procedure is used to efficiently and simultaneously generate the geometry and the high-resolution body-fitted grid for both the outdoor and indoor environment. This procedure allows modelling complex geometries with full control over grid quality and grid resolution, contrary to standard semi-automatic unstructured grid generation procedures. It also provides a way to easily implement various changes in the model geometry and grid for parametric studies. As a case study, a parametric analysis of natural ventilation is performed for the geometrically complex Amsterdam ArenA stadium in the Netherlands. The turbulent wind flow and temperature distribution around and inside the stadium are solved with the 3D steady Reynolds-averaged Navier-Stokes equations. Special attention is given to CFD solution verification and validation. It is shown that small geometrical modifications can increase the ventilation rate by up to 43%. The coupled modelling approach and grid generation procedure presented in this paper can be used similarly for future studies of wind flow and related processes in complex urban environments.

Keywords: Integrated model; Grid generation technique; Computational Fluid Dynamics (CFD); Air quality; Air exchange rate; Outdoor and indoor air flow; Numerical simulation; Full-scale measurements; Cross-ventilation; Sports stadium; Model validation and solution verification.

1. Introduction

Wind flow in urban environments is an important factor for a large number of physical processes that can affect human health and comfort and the durability of man-made constructions. Examples are atmospheric transport and dispersion of solid, liquid and gaseous air pollutants (Britter and Hanna 2003, Meroney 2004, Gromke and Ruck 2007, 2009, Blocken et al. 2008, Mensink and Cosemans 2008, Berkowicz et al. 2008, Yang and Shao 2008), wind-driven rain (Choi 1993, Blocken and Carmeliet 2004, Persoon et al. 2008, Abuku et al. 2009), wind loading (Stathopoulos 1997, Nozu et al. 2008), pedestrian wind comfort (Blocken et al. 2004, Stathopoulos 2006, Yoshie et al. 2007, Tominaga et al. 2008a) and natural ventilation of buildings (Reichrath and Davies 2002, Mochida et al. 2006). Urban wind flow is very complex, and appropriate tools are required for characterisation of the flow and the related processes. Three main approaches can be distinguished: (1) on-site full-scale experiments; (2) reduced-scale wind tunnel measurements; and (3) numerical modelling with Computational Fluid Dynamics (CFD). As opposed to experiments, the main advantages of CFD are that it provides information on the relevant flow variables in the whole calculation domain (whole-flow field data), under well-controlled conditions and without similarity constraints. However, the accuracy of CFD is an important matter of concern. Care is required in the geometrical implementation of the model and in grid generation, and solution verification and validation studies are imperative. CFD validation for urban wind flow in turn requires high-quality full-scale or reduced-scale measurements to be compared with the simulation results.

The use of CFD in urban wind studies is receiving strong support from several international initiatives that specifically focus on the establishment of guidelines for such simulations (Franke et al. 2004, Franke et al. 2007,

¹ Twan van Hooff is a PhD student at both Eindhoven University of Technology and the Katholieke Universiteit Leuven.

* Corresponding author: Twan van Hooff, Building Physics and Systems, Eindhoven University of Technology, P.O. box 513, 5600 MB Eindhoven, the Netherlands. Tel: +31 (0)40 247 5877, Fax: +31 (0)40 243 8595. *E-mail address:* t.a.j.v.hooff@tue.nl

Yoshie et al. 2007, Tominaga et al. 2008b, Tamura et al. 2008). In addition, other guidelines, for more general CFD applications, are available (e.g., Casey and Wintergerste 2000). Other research efforts have focused on specific aspects for improving the quality of CFD simulations, such as those concerning the simulation of equilibrium atmospheric boundary layers in computational domains (e.g. Richards and Hoxey 1993, Blocken et al. 2007a, 2007b, Franke et al. 2007, Hargreaves and Wright 2007, Yang et al. 2009, Gorlé et al. 2009). Among others, the existing guidelines focus on the importance of grid quality, in terms of cell shape, cell size gradients and overall grid resolution, and on the importance of grid-sensitivity analysis and the assessment of discretisation errors (Franke and Frank 2008). Up to now however, the guidelines have paid relatively little attention to procedures to generate high-resolution and high-quality grids for application in complex urban environments.

Indoor natural ventilation refers to air exchange between the outdoor environment and an enclosed or semi-enclosed indoor environment by wind and/or local density differences (buoyancy). In general, there are two methods that can be used to model natural ventilation in an enclosure with CFD. The first is a “coupled” CFD simulation, in which both the outdoor and indoor air flow are modelled simultaneously and within the same computational domain. This method allows the proper calculation of air flow in the proximity of and through the ventilation openings. The main disadvantage of this method in urban applications is the large difference in geometrical length scales between the outdoor (urban) environment (1-5 km) and the ventilation openings (e.g., 0.01 – 1 m), resulting in a large and high-resolution grid, and thus in a relatively high computational cost. This is probably the reason why in the past, this method has only been used for relatively simple outdoor and indoor environments and relatively large ventilation openings (e.g., Jiang et al. 2003, Allocca et al. 2003, Evola and Popov 2006, Hu et al. 2008, Horan and Finn 2008). The very large grids that would be required for complex outdoor and indoor environments and/or for small ventilation openings can be avoided by resorting to “de-coupled” simulations. In this case, two separate simulations are conducted, one for the outdoor flow and one for the indoor flow, each in their own computational domain (Jiang and Chen 2002, Cook et al. 2003, Chen 2009). In the outdoor flow simulations, the ventilation openings are closed. The information obtained from the simulation of the outdoor flow (generally pressure coefficients at the positions of the openings) can be used as boundary condition for the simulation of the indoor flow. Although this is the standard approach for indoor ventilation studies, its accuracy can easily be compromised because of the simplifications involved. Often, only pressure is passed from outdoor to indoor environment by means of pressure coefficients at the boundary, and assumptions are made in terms of discharge coefficients and expansion coefficients (Cook et al. 2003).

A coupled approach is preferred for urban wind flow and indoor natural ventilation studies. Due to the large differences in geometrical length scales between the urban area (1 – 5 km) and the ventilation openings (down to 0.01 m), CFD is preferred over wind tunnel modelling. The reason is that accurate wind tunnel modelling with adherence to similarity criteria would likely be inhibited by Reynolds number effects near and in the narrow ventilation openings. In CFD, the large difference in scales requires a high-resolution grid with strong local refinements, without compromising overall grid quality. To the knowledge of the authors, coupled CFD simulations of urban wind flow and indoor natural ventilation in complex urban environments and for complex building geometries have not yet been performed. Similarly, to the knowledge of the authors, also efficient grid generation procedures for such cases have not yet been presented.

This paper presents a coupled CFD modelling approach for urban wind flow and indoor natural ventilation on a high-resolution grid. It employs a specific procedure to efficiently and simultaneously generate the geometry and the high-resolution body-fitted grid for both the outdoor and indoor environment, based on translation and rotation of pre-meshed cross-sections. The approach is demonstrated by application to the case of a large multifunctional stadium situated in an urban environment, in which natural ventilation is the only means to ensure indoor air quality. The turbulent wind flow and temperature distribution around and inside the stadium are solved with the 3D steady Reynolds-averaged Navier-Stokes (RANS) equations and the realizable $k-\varepsilon$ turbulence model, supplemented with the Boussinesq model for thermal effects. Special attention is given to CFD solution verification by grid-sensitivity analysis and to CFD validation with on-site full-scale wind velocity measurements. The coupled CFD modelling approach is used to analyse the ventilation rates for different alternative ventilation configurations, which are obtained by introducing small changes in the current geometry of the stadium. All these ventilation configurations are *a priori* embedded in the same grid, and can be turned on/off by deleting parts of the grid.

First, in section 2, the urban area and stadium of the case study are described. In section 3, some full-scale measurements of the indoor conditions and ventilation rates are briefly presented to demonstrate the insufficient natural ventilation in the current situation. In addition, four alternative ventilation configurations are presented. Section 4 describes the numerical model geometry of the stadium and its surroundings and the procedure to simultaneously generate this geometry and the high-resolution body-fitted grid. Section 5 contains the CFD validation study. The results of the CFD simulations for the different ventilation configurations are given in section 6. Finally, sections 7 (discussion) and 8 (conclusions) conclude the paper.

2. Case study: urban area and stadium

2.1. Urban area

The urban area considered in this study is part of the city of Amsterdam, which is located in the north-west of the Netherlands. The city and its surroundings are located on very flat terrain; height differences are limited to less than 6 m. The study focuses on the south-east part of Amsterdam, known as “Zuidoost”. It is one of the fifteen districts of Amsterdam and contains four residential areas and a business park. In addition to medium and high rise office buildings, the business park also contains a recreational area, called the “ArenA Boulevard” that includes the ArenA stadium (Fig. 1). This area of Amsterdam Zuidoost is still under development, and several new large and high-rise buildings are planned in the vicinity. The height of the current surrounding buildings varies from 12 m to a maximum of 95 m for the “ABN-AMRO” office building (see Fig. 1).

The aerodynamic roughness length y_0 of the surroundings, which is needed for the CFD simulations, is determined based on the updated Davenport roughness classification (Wieringa 1992). The area on the north side of the ArenA Boulevard can be classified as “closed terrain” due to the urban character that is present in a radius of 10 km upwind. The estimated y_0 for this area is 1.0 m (Fig. 2). The south side area of the ArenA Boulevard is not as rough as the north side due to the presence of agricultural and natural areas and can be characterised with an y_0 of 0.5 m (Fig. 2).

2.2. Stadium

The Amsterdam ArenA is a so-called *oval* stadium (Fig. 3a). The roof is dome shaped and can be closed by moving two large panels with a projected horizontal area of $110 \times 40 \text{ m}^2$ (L x W). The roof consists of a steel frame, largely covered with semi-transparent polycarbonate sheets, while steel sheets are applied at the edge of the roof until a distance of 18 m from the gutter. Fig. 3b provides an inside view of the stadium. The stand consists of two separate tiers and runs along the entire perimeter. Figs. 3c-e show a detailed plan view and the two cross-sections $\alpha\alpha'$ and $\beta\beta'$. The exterior stadium dimensions are $226 \times 190 \times 72 \text{ m}^3$ (L x W x H). The stadium has a capacity of 51,628 seated spectators and an interior volume of about $1.2 \times 10^6 \text{ m}^3$. Fig. 4a shows a cross-section of the stadium, in which different components can be distinguished, which are indicated with numbers. These components contain the different ventilation openings used in this study. Numbers 1 and 2 are the logistic rings in which facilities and the entrances to the interior stadium volume are situated. Number 3 is an elevated circulation deck that runs around the stadium. It serves as parking and logistics area and is known as the *ArenA deck*. Four large gates in the corners of the stadium (Fig. 3c, 4b) connect the ArenA deck (Fig. 3c, 4a, 4b) with the stadium interior. Each gate has a cross-section $L_g \times H_g = 6.2 \times 6.7 \text{ m}^2$ and can be individually opened and closed. Number 4 indicates a safety and facility ring that separates the stands from the pitch. This ring runs along the entire perimeter of the field and connects the four gates.

Natural ventilation can occur through the openings that are present in the envelope of the stadium. The ArenA has several of such openings. The semi-transparent roof is the largest potential opening. During concerts and other festivities however, which are usually held in the summer period, the roof is closed most of the time to provide shelter for the spectators and the technical equipment. When the roof is completely open, it is the largest opening ($4,400 \text{ m}^2$) in the stadium envelope. When it is closed, natural ventilation of the stadium can only occur through a few smaller openings. The four gates in the corners of the stadium (Fig. 4) together form the second largest (potential) opening ($4 \times 41.5 \text{ m}^2$). They are open most of the time, but are sometimes closed during concerts to limit noise nuisance for the surroundings. Additionally, two relatively narrow openings are present in the upper part of the stadium (Fig. 4a; numbers 6 and 7). The first opening is situated between the stand and the steel roof construction, and runs along the entire perimeter of the roof (Fig. 5a). The total surface area of this opening is 130 m^2 . The other opening is situated between the fixed and movable part of the roof (Fig. 5b). This opening is only present along the two longest edges of the stadium. The total surface area of this opening is about 85 m^2 . An overview of the present ventilation openings and their surface areas is provided in Table 1. Of these openings, only the roof and gates can be opened/closed. In the basic stadium configuration in this study, the roof is closed, and all other openings are open. Alternative configurations will be defined in section 3.2, in which either existing openings are enlarged or new openings are introduced at a few positions.

3. Case study problem statement and alternative ventilation configurations

3.1. Problem statement

The ArenA is a so-called multifunctional stadium. Nowadays, more and more sports stadia are designed to serve a multitude of purposes. Apart from sports events, they also host a wide variety of other activities, such as concerts, conferences and festivities. For this purpose, many of these stadia are equipped with a roof construction

that can be opened and closed depending on the weather conditions and the type of event. However, they are generally not equipped with HVAC systems to control the conditions of the very large indoor air volume (up to 10^6 m^3), which is also the case for the ArenA. Indoor air quality problems can occur for the configuration with closed roof because of the large number of spectators and insufficient natural ventilation. During summer, overheating can be an additional problem. In absence of HVAC systems, natural ventilation is the only means to ensure indoor air quality.

To analyse the indoor conditions and natural ventilation of the stadium (with closed roof) during summer, full-scale measurements were made of – among others – indoor and outdoor air temperature, irradiance of the sky and the air exchange rate of the large indoor volume. The measurements inside the stadium were made at four different positions (Fig. 3c-e). The outdoor air temperature was measured at the ArenA deck. The irradiance of the sky was measured with a pyranometer on the roof. Fig. 6 shows the measured irradiance E and the measured air temperature θ_a inside (position N2 in Fig. 3c-e) and outside the stadium on both a sunny day (July 18, 2007) and a cloudy day (July 20, 2007). The indoor air temperature on the sunny day was almost 6°C higher than the outdoor temperature, due to the combined effect of solar radiation and insufficient natural ventilation, whereas the indoor air temperature on the cloudy day was only about 2°C higher than the outdoor temperature.

In addition, measurements were also made of the air exchange rate (ACH – Air Changes per Hour) of the stadium with closed roof, based on CO_2 concentration measurements at the four different positions in the stadium on three consecutive concert nights (June 1st until June 3rd). These indicated that the ACH on these three nights, averaged over the four measurement positions, was 0.68, 0.68 and 0.66, respectively. The ASHRAE Standard 62.1 (2004) prescribes a minimum ventilation rate of $10.3 \text{ dm}^3/\text{s}$ per person for disco/dance floors. During the concerts in the ArenA on these three nights, approximately 50,000 spectators were present, resulting in a required ACH of 1.5 h^{-1} , which is more than twice as high as the measured ACH. The ventilation during concerts in the ArenA, with the roof closed, was therefore not sufficient on these evenings. Note that the intention of these measurements was to indicate the insufficient natural ventilation. They will not be used for CFD validation in this study.

3.2. Alternative ventilation configurations

The measurements indicated that overheating can occur in the stadium during the daytime, and that also during three consecutive concert evenings, the ACH was insufficient. Therefore, CFD simulations are performed in this study to further evaluate natural ventilation for the current stadium configuration and for four alternative ventilation configurations. The alternative configurations consist of one specific geometrical change made to the current stadium geometry with closed roof, except for the last configuration, which has an open roof. Combinations of these specific changes are not considered. Alternative configuration 1 has eight extra openings on the second tier with a surface area of $2 \times 1.2 \text{ m}^2$ (Fig. 7a-b). These openings are created by opening the large windows that are situated on the second tier for logistical purposes (Fig. 4a, number 1). Configuration 2 is the current geometry of the stadium, but with a larger opening at the intersection of the concrete stand and the roof. This is achieved by removing half of the steel sheets (Fig. 7c versus d). For configuration 3, the steel sheets are removed entirely (Fig. 7e). Finally, configuration 4 has an opened roof.

4. CFD simulation: geometry, computational grid and solution parameters

4.1. Model geometry and computational domain

The computational model of the stadium reproduces its geometrical complexity with high resolution, down to details of 0.02 m for the narrow ventilation openings. This is required to accurately model the flow through these openings (Fig. 5 and 7). Because data with such high resolution are not available from GIS and/or city databases, the construction drawings of the stadium were used. The buildings that are situated in a radius of 500 m from the stadium are modelled explicitly, by only by their main shape (Fig. 8a). Buildings that are located at a greater distance are modelled implicitly, by imposing an increased equivalent sand-grain roughness height k_s and roughness constant C_s at the bottom of the computational domain. These values are based on the aerodynamic roughness length y_0 of the terrain in and beyond the computational domain and on the relationship between k_s , C_s and y_0 for the specific CFD code (Blocken et al. 2007a).

The computational domain has dimensions $L \times W \times H = 2,900 \times 2,900 \times 908.5 \text{ m}^3$. The maximum blockage ratio is 1.6%, which is below the recommended maximum of 3% (Franke et al. 2007, Tominaga et al. 2008b). Franke et al. (2007) also state that the distance from the building to the side, to the inlet and to the top of the domain should be at least five times the height of the building and the distance from the building to the outlet should be fifteen times the height. These requirements are also fulfilled.

4.2. Computational grid

Due to the complex geometry of the stadium and the large difference between the smallest (0.02 m) and the largest (2,900 m) length scales in the domain, generating a computational grid with good quality is not straightforward. Because of the required detail, high resolution and high resolution gradients of the grid, a body-fitted (BF) grid is used. The quality of the grid in the immediate vicinity of the stadium is considered very important for the coupled simulation of urban wind flow and indoor natural ventilation. Standard automatic or semi-automatic generation of an unstructured grid allows insufficient control of local grid resolution, grid stretching, control volume skewness and aspect ratio. To allow full control over the grid quality, size and resolution, a specific procedure to efficiently and simultaneously generate the geometry and the computational grid is used here. It consists of a series of extrusion operations, i.e. creating the geometry and the grid based on geometrical translation and rotation operations of pre-meshed 2D cross-sections. The procedure is schematically depicted in Fig. 9a. It consists of the following steps:

1. Creating the geometry and the grid of the vertical stadium cross-section (indicated by “1” in Fig. 9a). Both the solid and fluid parts of this cross-section are meshed;
2. Defining a line A in the ground plane which represents the inner stadium circumference, and applying a grid to this line;
3. Sweeping cross-section “1” (geometry and grid) along line A. This way, both the geometry and the volume grid of the stadium circumference are generated. The volume grid is generated based on the cross-section grid and the grid on line A. Note that at this stage, both solid and fluid volumes are meshed;
4. Applying a grid to the bounded plane “2”, which is that part of the ground plane of which line 1 represents the circumference; this plane represents the stadium interior;
5. Sweeping plane “2” (geometry and grid) vertically along line B. This way, both the geometry and the volume grid of the stadium interior are generated, up to the end position of line B;
6. Defining all lines in the ground plane outside the stadium that represent the circumference of the surrounding buildings, streets and squares. The outermost lines are the bounds of the bottom of the computational domain;
7. Applying a surface grid to the collection of planes “3” that are bounded by these lines;
8. Sweeping all planes “3” (geometry and grid) vertically along line C.
9. Defining a line D which starts at the top of the stadium cross-section, defined in step 1, and ends at the roof height of the lowest building that is higher than the end point of line B. Defining a line E which starts at the end point of line D, and ends at the roof height of the lowest building that is higher than the end point of line D, and so on for lines F, G, etc., up to the intended height of the computational domain;
10. Sweeping all horizontal planes (geometry and grid) at the height of the starting point of line D vertically along line D, next along line E, and so on. The final sweep also generates the top surface of the domain. The result is a rectangular prism (the computational domain) that is completely meshed and that contains all buildings;
11. Deleting the grid at the location of the intended solid domain parts (buildings and building parts). This way, solid volumes are introduced and only the fluid domain remains meshed.

Fig. 9b illustrates the application of this procedure for the actual stadium geometry by showing a few cross-sections and part of the generated volume grids. The advantages of this systematic procedure are: (1) Simultaneous generation of geometry and grid for both the outdoor and indoor environment; (2) Full control over grid generation yielding a BF grid without tetrahedral cells; (3) The possibility to a priori implement different geometrical variations in the model/grid (which will be explained below).

The procedure was executed with the aid of the pre-processor Gambit 2.4.6, resulting in a hybrid grid with about 5.6×10^6 prismatic and hexahedral cells. An overall view of the grid from northeast is shown in Fig. 8b, and more detailed views are given in Figs. 10 and 11. Special attention was paid to providing a high grid resolution in and around the ventilation openings in the facade of the stadium, as well as in and around the new ventilation openings mentioned in section 3.2. Because of the complex geometry of the stadium and the large domain that is used, some parts of the stadium that are less important for the flow through the ventilation openings have a slightly coarser grid, as well as the buildings that are not in the close proximity of the stadium. Fig. 10a shows the computational grid at the deck on the east side of the stadium, and Fig. 10b shows the corresponding picture of this part of the stadium. Comparing Fig. 10a and b shows that some of the exterior support structures are not included in the model. The reason is that these slender structures are located at a relatively large distance from the gates (40 m) and that they do not extend up to the position of the roof ventilation openings (Fig. 4a, number 6, and Fig. 5a). Note that the triangular shapes in Fig. 10a are the

footprints of prisms, and not of tetrahedral cells. These prisms are created by sweeping an unstructured triangle-meshed cross-section, as explained above. Fig. 11 provides a bird-eye view, showing the grid at the roof, the roof gutter (see also Fig. 5a) and the deck.

A grid-sensitivity analysis is performed for the current configuration (roof closed, gates open) by making two new grids, a coarser grid with 3.0 million cells and a finer grid with 9.2 million cells. The minimum volumes for the three grids are $4.3 \times 10^{-5} \text{ m}^3$, $3.5 \times 10^{-5} \text{ m}^3$ and $2.0 \times 10^{-5} \text{ m}^3$. The grid-sensitivity analysis is best performed by comparing relevant parameters at relevant locations. In this paper, the different ventilation configurations will be evaluated and compared based on the overall ventilation rate/ACH of the entire indoor air volume. The ACH will be calculated based on the mass flow rates through the ventilation openings. Therefore, the most relevant locations are the ventilation openings, and the most relevant parameter is the mass flow rate through these openings. A more detailed grid-sensitivity analysis could also focus on point wind speed values in these openings or wind speed profiles through the openings. This would be important when the wind speed distributions across the openings and inside the stadium volume are of interest, such as for local human comfort studies. This is however outside the scope of the present paper. The three grids are therefore compared based on the normalised mass flow rates through the four gates:

$$\delta_1 = \sum_{i=1}^4 \left| \frac{m_{i;coarse} - m_{i;middle}}{m_{total;middle}} \right| \times 100\% \quad (1)$$

$$\delta_2 = \sum_{i=1}^4 \left| \frac{m_{i;middle} - m_{i;fine}}{m_{total;fine}} \right| \times 100\% \quad (2)$$

where $m_{i;coarse}$, $m_{i;middle}$ and $m_{i;fine}$ are the mass flow rates (kg/s) through gate i for the coarse, middle and fine grid, respectively. δ_1 is 4.7% and δ_2 is 2.0%. The results obtained with the middle grid show no large discrepancies with the results of the finer one. The results obtained with the coarse grid show somewhat larger deviations from the middle grid. Therefore, the middle grid was selected. Note that the specific grid generation procedure for the case of this stadium does not allow the use of a systematic identical refinement factor throughout the entire domain. As a result, the discretisation errors themselves have not been determined.

As mentioned above, an extra advantage of this grid generation technique is the possibility to a priori implement different geometrical variations in the model/grid. This allows to easily generate a range of different models and grids without having to rebuild them all from the start. By defining extra meshed volumes in the model, one can change the building geometry by just deleting the volumes that have to become solid, i.e. part of the building. An example of such a geometrical change is shown in Fig. 12, in which the ventilation opening between the fixed and movable part of the roof is shown. In order to close these openings, the meshed volumes that are indicated with numbers 1, 2 and 3 are removed (Fig. 12a). It is also possible to add extra ventilation openings or increase existing openings by removing less meshed volumes (Fig. 12b). This strategy has been used for all ventilation configurations in this study.

4.3. Boundary conditions

At the inlet of the domain, a logarithmic mean wind speed profile representing a neutral atmospheric boundary layer is imposed with $y_0 = 0.5 \text{ m}$ or 1.0 m , dependent on the wind direction (see Fig. 2), and a reference wind speed U_{10} (at 10 m height) of 5 m/s. For $y_0 = 0.5 \text{ m}$, the inlet longitudinal turbulence intensity I_u ranges from 30 % at pedestrian height ($y = 2 \text{ m}$) to 5 % at gradient height. For $y_0 = 1 \text{ m}$, I_u ranges from 40 % ($y = 2 \text{ m}$) to 8 % at gradient height. Turbulent kinetic energy k is calculated from I_u using $k = 1.5(I_u U)^2$, assuming isotropic turbulence. The turbulence dissipation rate $\varepsilon = (u_{ABL}^*)^3 / (\kappa(y + y_0))$, where y is the height coordinate, κ the von Karman constant ($\kappa = 0.42$) and u_{ABL}^* the atmospheric boundary layer (ABL) friction velocity related to the logarithmic mean wind speed profile.

The standard wall functions by Launder and Spalding (1974) are used with the sand-grain based roughness modification by Cebeci and Bradshaw (1977). The parameters k_s and C_s in the roughness modification, as implemented in Fluent (Fluent Inc. 2006), are determined from their appropriate relationship with y_0 . This relationship was derived by Blocken et al. (2007a) for Fluent and CFX. For Fluent 6, up to at least version 6.3, it is given by:

$$k_s = \frac{9.793 y_0}{C_s} \quad (3)$$

Note that for fully rough walls, only the product $k_s C_s$ occurs in the wall functions, and therefore only the value of the product and not of the individual parameters k_s and C_s is important. Note that Fluent 6 (up to at least version 6.3) does not allow k_s to be larger than y_p , which is the distance between the centre point of the wall-adjacent cell and the wall. If the user implements a larger value, the code will automatically set k_s equal to y_p without warning. Therefore, in this study, k_s is taken smaller than or equal to y_p and C_s is chosen to satisfy Eq. (3). A user-defined function setting the value of the constant C_s is required because the Fluent 6.3 code does not allow it to exceed the interval $[0;1]$ otherwise. For the ground surface with implicitly modelled buildings, k_s is taken 0.7 m and $C_s = 7$ for $y_0 = 0.5$ m. For $y_0 = 1.0$ m, $k_s = 1.4$ m and $C_s = 7$. For the ground surface in the direct vicinity around the explicitly modelled buildings and the stadium, $y_0 = 0.03$ m is taken, which is imposed by setting $k_s = 0.59$ m and $C_s = 0.5$. The building surfaces are set to have zero roughness height ($k_s = 0$). Zero static pressure is imposed at the outlet. The top of the computational domain is modelled as a slip wall (zero normal velocity and zero normal gradients of all variables).

Two sets of simulations are performed: (1) isothermal CFD simulations for the validation study based on wind velocity measurements (section 5); and (2) thermal CFD simulations for the analysis of natural ventilation on a typical warm summer day (section 6). The isothermal simulations are justified due to the strong winds and cloudy conditions on the days of the wind velocity measurements. For the thermal simulations, an important remark has to be made. The intention of these simulations was to compare the performance of the different ventilation configurations under simplified boundary conditions for a warm summer day. The intention was not to reproduce the full complexity of the transient thermal behaviour of the stadium under transient meteorological conditions and internal heat, vapour and CO_2 production by spectators and equipment. This would require either transient CFD simulations for a period of several days, which is out of reach given the need for short time steps in CFD, or the need to couple CFD simulations to Building Energy Simulation Software (e.g., Hensen 2004, Djunaedi et al. 2005). To compare the performance of the different ventilation configurations, the thermal boundary conditions are simplified and are taken constant in time. The temperature of the inlet air is set to 20°C . To take into account the increased air temperature inside the stadium as a result of solar radiation, estimated surface temperatures are imposed on the surfaces inside the stadium. These surface temperatures vary from 22°C for the semi-transparent roof to 50°C for the steel sheets covering the pitch during summer for conferences and other events. They yield a stationary indoor air temperature of about 30° . Note that, because the intention of the simulations is not to reproduce the actual transient conditions during one specific period of time, the simulated ACH values can not be compared to the measured ones that were mentioned in section 3.1.

4.4. Other computational parameters

The 3D steady RANS equations are solved in combination with the realizable k - ϵ turbulence model (Shih et al. 1995) using the commercial CFD code Fluent 6.3.26 (Fluent Inc. 2006). The realizable k - ϵ turbulence model is chosen because of its general good performance for wind flow around buildings (Franke et al. 2004) and the overall good performance of k - ϵ models for indoor air flow (Linden 1999, Sorensen and Nielsen 2003). Pressure-velocity coupling is taken care of by the SIMPLE algorithm, pressure interpolation is standard and second order discretisation schemes are used for both the convection terms and the viscous terms of the governing equations. The Boussinesq approximation is used for buoyancy, which is valid because $\beta(T-T_0) = 0.07 \ll 1$, where β is the thermal expansion coefficient and $T-T_0$ the maximum temperature difference. Radiation does not need to be taken into account because temperatures are imposed on all surfaces inside the stadium.

The computations were performed using parallel processing on a Sun Fire X4150 server containing two Quad-Core Intel Xeon E5440 2.83 GHz processors and 16 GB Fully Buffered DDR2 memory. The simulations were terminated after 6000 iterations with a total duration of 48 hours, when additional iterations showed no further convergence. The scaled residuals (Fluent Inc. 2006) reached the following minimum values: 10^{-7} for x , y and z velocity, 10^{-6} for k and ϵ , 10^{-8} for energy and 10^{-5} for continuity.

5. CFD validation

For CFD validation purposes, the 3D wind velocity in and around the stadium was measured in the period September-November 2007, on days with strong winds (reference wind speed U_{ref} above 8 m/s). Measurements were made with ultrasonic anemometers, positioned on mobile posts, at a height of 2 m above the ArenA deck. Reference wind speed (U_{ref}) was measured on top of a 10 m mast on the roof of the 95 m high ABN-AMRO office building, which is the highest building in the proximity of the stadium (Fig. 1). The data were sampled at 5 Hz, averaged into 10-minute values and analysed. Only data with at least 12 different 10-minute values per wind direction sector of 10° were retained. The measured wind speed U at the locations in the four gates (Fig. 13) was divided by the reference wind speed U_{ref} measured on top of the ABN-AMRO office building. Note that the term “wind speed” refers to the magnitude of the 3D mean wind velocity vector. This wind speed ratio is also

calculated with CFD and both ratios are compared. Also the measured and calculated local wind directions at the stadium measurement positions are compared.

Two wind directions and configurations are considered. The validation for $\varphi = 228^\circ$ is performed for a closed roof, and that for $\varphi = 350^\circ$ with open roof. Fig. 14a compares simulated and measured mean wind speed ratios for $\varphi = 228^\circ$ and closed roof, indicating a rather good agreement. Significant wind speed gradients exist at the measurement position D. As a result, a small shift in measurement position or a small change in the flow field can significantly affect the simulation values at this position. To indicate this effect, the deviations in simulated wind speed by a 0.5 m shift in position are indicated by “error bars”. Note however that in many cases, the gradients are too small for the error bars to be visible. A good agreement between measurements and simulations is also found for the local wind direction in the gates (Fig. 14b), except for gate D, where a deviation of 30% is found. Fig. 14c shows the results for $\varphi = 350^\circ$ and open roof. The results for the wind speed show a fair to good agreement (Fig. 14c), while those for local wind direction are good for gates A and B, but less good for gates C (50% deviation) and D (22% deviation) (Fig. 14d). This might be attributed to the fact that both positions are in the wake of the stadium for $\varphi = 350^\circ$. Note that while at first sight the discrepancy for gate B in Fig. 14d might seem to be large, the actual difference between measured value (8°) and simulated value (340°) and is only 28° . Overall, a fair to good agreement is obtained for the simulations, and the stadium model is used to evaluate different ventilation configurations.

6. CFD results for natural ventilation

Thermal simulations were performed for two wind directions perpendicular to the north and south facade of the stadium (151° and 331°) and for two wind directions under an angle of 45° with the stadium facade (16° and 196°) (Fig. 15a). For $\varphi = 16^\circ$ and 331° , no immediate buildings are present upstream of the stadium, as opposed to $\varphi = 151^\circ$ and 196° . The reference wind speed U_{10} (at 10 m height) is 5 m/s for all simulations, and the thermal boundary conditions are as described in section 4.3. The effectiveness of the different ventilation configurations is assessed using the air exchange rate, as defined by ASHRAE (2005):

$$ACH = \frac{Q}{V} \quad (4)$$

where Q is the volumetric air flow rate into the enclosure (m^3/s) and V the volume of the enclosure (m^3). For each ventilation configuration, the simulated mass flow rates through each opening are used to determine the ACH using Eq. (4). The results of the calculations are shown in Table 2 and indicate that opening the windows on the second tier only increases the ACH on average from 1.36 h^{-1} to 1.38 h^{-1} . Configurations 2 and 3 seem more useful: removing half of the steel sheets increases the ACH on average by 17%, while removing the entire steel sheets increases it on average by 43%. Furthermore, opening the roof provides an average increase with 158% to 3.51 h^{-1} . The results also show that the ACH strongly depends on the wind direction. The lowest air exchange rates are present for $\varphi = 196^\circ$, which is the wind direction with a group of buildings present upstream of the stadium, which provide some shelter from wind. The deviations in ACH between $\varphi = 16^\circ$ (exposed) and $\varphi = 196^\circ$ (sheltered) for the current configuration and for configurations 1, 2, 3 and 4 are 26%, 28%, 32%, 26% and 42%, respectively. This demonstrates the importance of modelling the surrounding urban environment for natural ventilation analysis. Figs. 15b-d show the contours of the non-dimensional velocity magnitude U/U_{10} around the ArenA for $\varphi = 196^\circ$ (SSW) in horizontal planes at heights of 10, 20, 40 and 60 m above the ArenA deck, at which the lowest openings (gates) are situated. The lower values around the ArenA indicate that the stadium is indeed situated in the wake of the office buildings, causing the lower ACH for this wind direction. Note that this (SW) is the prevailing wind direction in the Netherlands.

7. Discussion

A coupled modelling approach for urban wind flow and indoor natural ventilation on a high-resolution grid has been presented. The approach has been applied to analyse natural ventilation in the geometrically complex Amsterdam ArenA stadium.

A few important remarks have to be made. The thermal simulations have been performed in steady-state with fixed surface temperatures. The intention of these simulations was only to demonstrate the coupled approach and to provide a first comparative evaluation of different ventilation configurations. The intention was not to accurately model the transient thermal behaviour of the indoor stadium volume. This would require either transient CFD simulations for a period of several days, which is out of reach given the need for short time steps in CFD, or coupling these CFD simulations to thermal Building Energy Simulation software, which is a topic for future research. The full-scale measurements of temperature and ACH in the stadium were only performed to

indicate the occurrence of overheating and insufficient natural ventilation episodes in the stadium. Because these measurements are the result of, among others, transient thermal processes throughout the day and the previous days, they cannot be used for validation of the steady-state CFD simulations. This is the reason why an alternative validation study was conducted, based on full-scale wind speed measurements on cloudy and windy days, on which thermal effects (natural convection) were negligible compared to wind-induced effects (forced convection). In such cases, the wind speed spectrum of van der Hoven (1957) indicates stationarity in the spectral gap and 10-minute wind speed measurements are often used to validate steady-state CFD simulations.

Further research is also needed on several other topics. The steady RANS simulations performed in this study have shown a fair to good agreement with on-site outdoor wind velocity measurements, but also some discrepancies. These can possibly be attributed to the inability of steady RANS to simulate inherently transient effects in urban aerodynamics such as the collapse of separation and recirculation regions and vortex shedding in the wake of bluff obstacles. Future work will focus on LES simulations to assess the impact of these features on the ventilation results.

The comparison of the ventilation configurations was performed for only one reference wind speed $U_{10} = 5$ m/s. While this provides a first, limited indication of their relative performance, a more detailed evaluation needs to consider different reference wind speed values to generate results for a range of Archimedes numbers. The interaction between forced and natural convection in natural ventilation (Linden 1999) remains an important topic for future research. To provide some information on the relative importance of forced (wind) versus natural (buoyancy) convection, simulations for the basic stadium configuration (closed roof) were also made with the same reference wind speed of 5 m/s, but in isothermal conditions. For $\varphi = 151^\circ$, the ACH drops from 1.33 to 0.77h^{-1} , and for $\varphi = 196^\circ$ it drops from 1.11 to 0.63h^{-1} . For these wind directions, including thermal effects as implemented in this study almost doubles the ACH.

In this study, only the overall ventilation rate/ACH of the entire indoor volume has been used as a parameter for the evaluation of the different alternative ventilation configurations. Future studies will also focus on the indoor air speed and temperature distribution, which is necessary for e.g. local human comfort assessment in the stadium. The grid-sensitivity analysis in that case will also need to focus on – among others – the distribution of wind speed in the indoor volume, rather than only on mass flow rates through the openings, as done in this paper. Especially in this situation, it would also be important to gather wind speed measurements at more locations in the ventilation openings for CFD validation, as well as to gather more indoor climate measurements.

8. Summary and conclusions

A coupled CFD modelling approach for urban wind flow and indoor natural ventilation on a high-resolution grid has been presented. It is specifically intended for studies with large differences in geometrical length scales between the urban area (1 – 5 km) and the natural ventilation openings (down to 0.01 m). The approach has been applied to analyse natural ventilation for the geometrically complex Amsterdam ArenA stadium, with length scales ranging from 2,900 m to 0.02 m. CFD modelling is preferred for such studies, because accurate wind tunnel modelling with adherence to similarity criteria would likely be inhibited by Reynolds number effects near and in the narrow ventilation openings.

The coupled approach implies that the outdoor and the indoor air flow are solved simultaneously and within the same computational domain. The advantage of this approach is that no assumptions have to be made at the interface between outdoor and indoor environment; the flow through the ventilation openings is solved explicitly and all flow variables are directly transferred between the outdoor and indoor parts of the domain.

This paper has presented a specific procedure to efficiently and simultaneously generate the geometry and the high-resolution body-fitted (BF) grid based on translation and rotation of pre-meshed cross-sections. This procedure provides several advantages: (1) Simultaneous generation of geometry and grid for both the outdoor and indoor environment for coupled outdoor-indoor studies; (2) Full control by the user over grid quality and grid resolution; (3) The possibility to implement different geometric variations in the model/grid such as new ventilation openings, additional surrounding buildings, etc. and to use this to easily generate different grids for parametric studies. This can significantly reduce pre-processing times for parametric studies.

The coupled approach and grid generation procedure have been applied for a parametric study of natural ventilation of the multifunctional Amsterdam ArenA stadium in the Netherlands. The stadium has a retractable roof, which is closed during concerts and festivities. In this case, natural ventilation can only occur through the limited number of openings in the stadium envelope. Full-scale measurements indicated that in this configuration, overheating can occur during summer because the natural ventilation is insufficient to remove warm air during the day. Furthermore, the CO_2 measurements showed that the air exchange rate (ACH) on three concert evenings did not meet the ASHRAE ventilation requirements.

To analyse the natural ventilation of the stadium, coupled 3D steady RANS CFD simulations were performed on a high-resolution BF grid with 5.6 million prismatic and hexahedral cells. Closure was obtained using the realizable k- ϵ model. Specific attention was paid to CFD solution verification and validation. The grid was based

on grid-sensitivity analysis and validation was performed based on on-site full-scale measurements of wind speed in the gates of the stadium.

Natural ventilation was evaluated for the current situation and for four alternative ventilation configurations, using CFD simulations of non-isothermal mixing ventilation on a warm summer day. Five different geometries and grids were used, which were all generated based on the same computational grid by simply deleting (or non deleting) meshed volumes. The simulations showed that, for the meteorological conditions under study, increasing the size of specific openings near the roof can increase the air exchange rate by up to 43%. Large differences in ACH were found depending on wind direction. The values for SSW wind, with a group of buildings upstream, are up to 42% lower than those for NNE wind, without buildings upstream. This demonstrates the importance of modelling the surrounding urban environment for natural ventilation analysis.

Future research will focus on – among others – combining the CFD simulations with Building Energy Simulation software to analyse the actual transient thermal behaviour of the large stadium air volume throughout several days/weeks. Further work will also include the evaluation of steady RANS, LES and various types of wall functions for natural mixing ventilation studies of large enclosures in urban environments, and the analysis of indoor air speed, temperature, relative humidity and CO₂ distributions.

Acknowledgements

The first author is currently a PhD student funded by both Eindhoven University of Technology in the Netherlands and the Katholieke Universiteit Leuven in Flanders, Belgium. The work in this paper was performed during his previous period at Eindhoven University of Technology.

The measurements reported in this paper were supported by the Laboratory of the Unit Building Physics and Systems (BPS) of Eindhoven University of Technology. Special thanks go to Ing. Jan Diepens, head of LBPS, and Ing. Harrie Smulders, Wout van Bommel and GeertJan Maas, members of the LBPS, for their important contribution. We also thank Martin Wielaart, manager at the Amsterdam ArenA for his help during the measurements, and the anonymous reviewers for their valuable comments.

References

- Abuku, M., Blocken, B., Nore, K., Thue, J.V., Carmeliet, J., Roels, S., 2009. On the validity of numerical wind-driven rain simulation on a rectangular low-rise building under various oblique winds. *Building and Environment* 44(3) 621– 632.
- Allocca, C., Chen, Q., Glicksman, L.R., 2003. Design analysis of single-sided natural ventilation. *Energy and Buildings* 35(8) 785-795.
- ASHRAE, 2004. ASHRAE Standard 62.1-2004. Ventilation for acceptable indoor air quality, American Society of Heating, Refrigerating and Air-Conditioning Engineers, Atlanta, GA, USA.
- ASHRAE, 2005. Handbook of Fundamentals. American Society of Heating, Refrigerating and Air-Conditioning Engineers, Inc., Atlanta, USA.
- Berkowicz, R., Ketzel, M., Jensen, S.S., Hvidberg, M., Raaschou-Nielsen, O., 2008. Evaluation and application of OSPM for traffic pollution assessment for a large number of street locations. *Environmental Modelling & Software* 23(3) 296-303.
- Blocken, B., Carmeliet, J. 2004. A review of wind-driven rain research in building science. *Journal of Wind Engineering and Industrial Aerodynamics* 92(13) 1079-1130.
- Blocken, B., Roels, S., Carmeliet, J., 2004. Modification of pedestrian wind comfort in the Silvertop Tower passages by an automatic control system. *Journal of Wind Engineering and Industrial Aerodynamics* 92(10) 849-873.
- Blocken, B., Stathopoulos, T., Carmeliet, J., 2007a. CFD simulation of the atmospheric boundary layer: wall function problems. *Atmospheric Environment* 41(2) 238-252.
- Blocken, B., Carmeliet, J., Stathopoulos, T., 2007b. CFD evaluation of wind speed conditions in passages between parallel buildings—effect of wall-function roughness modifications for the atmospheric boundary layer flow. *Journal of Wind Engineering and Industrial Aerodynamics* 95(9-11) 941-962.
- Blocken, B., Stathopoulos, T., Saathoff, P., Wang, X., 2008. Numerical evaluation of pollutant dispersion in the built environment: comparisons between models and experiments. *Journal of Wind Engineering and Industrial Aerodynamics* 96(10-11) 1817-1831.
- Britter R.E., Hanna S.R., 2003. Flow and dispersion in urban areas. *Annual Review of Fluid Mechanics* 35 469-496.
- Casey, M., Wintergerste, T. (Eds), 2000. Best Practice Guidelines, ERCOFTAC Special Interest Group on Quality and Trust in Industrial CFD, ERCOFTAC, Triomflaan 43, B-1160, Brussels
- Cebeci, T., Bradshaw, P., 1977. Momentum transfer in boundary layers, Hemisphere Publishing Corporation,

- Chen, Q., 2009. Ventilation performance prediction for buildings: A method overview and recent applications. *Building and Environment* 44(4) 848-858.
- Choi, E.C.C., 1993. Simulation of wind-driven rain around a building. *Journal of Wind Engineering and Industrial Aerodynamics* 46&47 721-729.
- Cook, M.J., Ji, Y., Hunt, G.R., 2003. CFD modeling of natural ventilation: combined wind and buoyancy forces. *International Journal of Ventilation* 1(3) 169-180.
- Djunaedy, E., Hensen, J.L.M., Loomans, M., 2005. External coupling between CFD and energy simulation: implementation and validation. *ASHRAE Transactions, American Society of Heating, Refrigerating, and Air-Conditioning Engineers* 109 612-624.
- Evola, G., Popov, V., 2006. Computational analysis of wind driven natural ventilation in buildings. *Energy and Buildings* 38(5) 491-501.
- Fluent Inc., 2006. *Fluent 6.3 User's Guide*. Fluent Inc., Lebanon.
- Franke, J., Frank, W., 2008. Application of generalized Richardson extrapolation to the computation of the flow across an asymmetric street intersection. *Journal of Wind Engineering and Industrial Aerodynamics* 96(10-11) 1616-1628.
- Franke, J., Hellsten, A., Schlünzen, H., Carissimo, B. (Eds.), 2007. *Best practice guideline for the CFD simulation of flows in the urban environment*. COST Office Brussels, ISBN 3-00-018312-4.
- Franke, J., Hirsch, C., Jensen, A.G., Krüs, H.W., Schatzmann, M., Westbury, P.S., Miles, S.D., Wisse, J.A., Wright, N.G., 2004. Recommendations on the use of CFD in wind engineering. In: van Beeck, J.P.A.J. (Eds.), *Proceedings of the International Conference on Urban Wind Engineering and Building Aerodynamics*. COST Action C14, Impact of Wind and Storm on City Life Built Environment. Von Karman Institute, Sint-Genesius-Rode, Belgium, 5-7 May 2004.
- Gorlé, C., van Beeck, J., Rambaud, P., Van Tendeloo, G., 2009. CFD modelling of small particle dispersion: the influence of the turbulence kinetic energy in the atmospheric boundary layer. *Atmospheric Environment* 43(3) 673-681.
- Gromke, C., Ruck, B., 2007. Influence of trees on the dispersion of pollutants in an urban street canyon—Experimental investigation of the flow and concentration field. *Atmospheric Environment* 41(16) 3287-3302.
- Gromke, C., Ruck, B., 2009. On the impact of trees on dispersion processes of traffic emissions in street canyons. *Boundary-Layer Meteorology* 131(1) 19-34.
- Hargreaves, D.M., Wright, N.G., 2007. On the use of the $k-\epsilon$ model in commercial CFD software to model the neutral atmospheric boundary layer. *Journal of Wind Engineering and Industrial Aerodynamics* 95(5) 355-369.
- Hensen, J.L.M., 2004. Integrated building airflow simulation. In: Malkawi, A., Augenbroe, G., (Eds.), *Advanced Building Simulation*. Spon Press, New York, 87-118.
- Horan, J.M., Finn, D.P. 2008. Sensitivity of air change rates in a naturally ventilated atrium space subject to variations in external wind speed and direction. *Energy and Buildings* 40(8) 1577-1585.
- Hu, C-H., Ohba, M., Yoshie, R., 2008. CFD modelling of unsteady cross ventilation flows using LES. *Journal of Wind Engineering and Industrial Aerodynamics* 96(10-11) 1692-1706.
- Jiang, Y., Chen, Q., 2002. Effect of fluctuating wind direction on cross natural ventilation in buildings from large eddy simulation. *Building and Environment* 37(4) 379-386.
- Jiang, Y., Alexander, D., Jenkins, H., Arthur, R., Chen, Q., 2003. Natural ventilation in buildings: Measurement in a wind tunnel and numerical simulation with large-eddy simulation. *Journal of Wind Engineering and Industrial Aerodynamics* 91(3) 331-353.
- Launder, B.E., Spalding, D.B., 1974. The numerical computation of turbulent flows. *Computer Methods in Applied Mechanics and Engineering* 3 269-289.
- Linden, P.F., 1999. The fluid mechanics of natural ventilation, *Annual Review of Fluid Mechanics* 31 pp. 201-238.
- Mensink, C., Cosemans, G., 2008. From traffic flow simulations to pollutant concentrations in street canyons and backyards. *Environmental Modelling & Software* 23(3) 288-295.
- Meroney, R.N., 2004. Wind tunnel and numerical simulation of pollution dispersion: a hybrid approach. Working paper, Croucher Advanced Study Institute on Wind Tunnel Modeling, Hong Kong University of Science and Technology, 6-10 December, 2004, 60 pp.
- Mochida, A., Yoshino, H., Miyauchi, S., Mitamura, T., 2006. Total analysis of cooling effects of cross-ventilation affected by microclimate around a building. *Solar Energy* 80(4) 371-382.
- Nozu, T., Tamura, T., Okuda, Y., Sanada, S., 2008. LES of the flow and building wall pressures in the center of Tokyo. *Journal of Wind Engineering and Industrial Aerodynamics* 96(10-11) 1762-1773.
- Persoon, J., van Hooff, T., Blocken, B., Carmeliet, J., de Wit, M.H., 2008. On the impact of roof geometry on rain shelter in football stadia. *Journal of Wind Engineering and Industrial Aerodynamics* 96(8-9) 1274-1293.
- Reichrath, S., Davies, T.W., 2002. Using CFD to model the internal climate of greenhouses: past, present and future. *Agronomie* 22(1) 3-19.

- Richards, P.J., Hoxey, R.P., 1993. Appropriate boundary conditions for computational wind engineering models using the k- ϵ turbulence model. *Journal of Wind Engineering and Industrial Aerodynamics* 46&47 145-153.
- Shih, T.-H., Liou, W.W., Shabbir, A., Zhu, J., 1995. A new k- ϵ eddy-viscosity model for high Reynolds number turbulent flows—model development and validation. *Computers and Fluids* 24 (3) 227–238.
- Sorensen, D.N., Nielsen, P.V., 2003. Quality control of computational fluid dynamics in indoor environments. *Indoor Air* 13: 2-17.
- Stathopoulos, T. 2006. Pedestrian level winds and outdoor human comfort. *Journal of Wind Engineering and Industrial Aerodynamics* 94(11) 769-780.
- Stathopoulos, T., 1997. Computational wind engineering: Past achievements and future challenges. *Journal of Wind Engineering and Industrial Aerodynamics* 67-68 509-532.
- Tamura, T., Nozawa, K., Kondo, K., 2008. AIJ guide for numerical prediction of wind loads on buildings. *Journal of Wind Engineering and Industrial Aerodynamics* 96(10-11) 1974-1984.
- Tominaga, Y., Mochida, A., Murakami, S., Sawaki, S., 2008a. Comparison of various revised k- ϵ models and LES applied to flow around a high-rise building model with 1:1:2 shape placed within the surface boundary layer. *Journal of Wind Engineering and Industrial Aerodynamics* 96(4) 389-411.
- Tominaga, Y., Mochida, A., Yoshie, R., Kataoka, H., Nozu, T., Yoshikawa, M., Shirasawa, T. 2008b. AIJ guidelines for practical applications of CFD to pedestrian wind environment around buildings. *Journal of Wind Engineering and Industrial Aerodynamics* 96(10-11) 1749-1761.
- Van der Hoven, I., 1957. Power spectrum of horizontal wind speed in the frequency range from 0.0007–900 cycles per hour. *Journal of Meteorology*. 14, 160–164.
- Wieringa, J. 1992. Updating the Davenport roughness classification. *Journal of Wind Engineering and Industrial Aerodynamics* 41(1) 357-368.
- Yang, Y., Gu, M., Chen, S., Jin, X., 2009. New inflow boundary conditions for modelling the neutral equilibrium atmospheric boundary layer in computational wind engineering. *Journal of Wind Engineering and Industrial Aerodynamics* 97(2) 88-95.
- Yang, Y., Shao, Y., 2008. Numerical simulations of flow and pollution dispersion in urban atmospheric boundary layers. *Environmental Modelling & Software* 23(7) 906-921.
- Yoshie, R., Mochida, A., Tominaga, Y., Kataoka, H., Harimoto, K., Nozu, T., Shirasawa, T., 2007. Cooperative project for CFD prediction of pedestrian wind environment in the Architectural Institute of Japan. *J. Wind Eng. Ind. Aerodyn.* 95(9-11) 1551-1578.

Figures

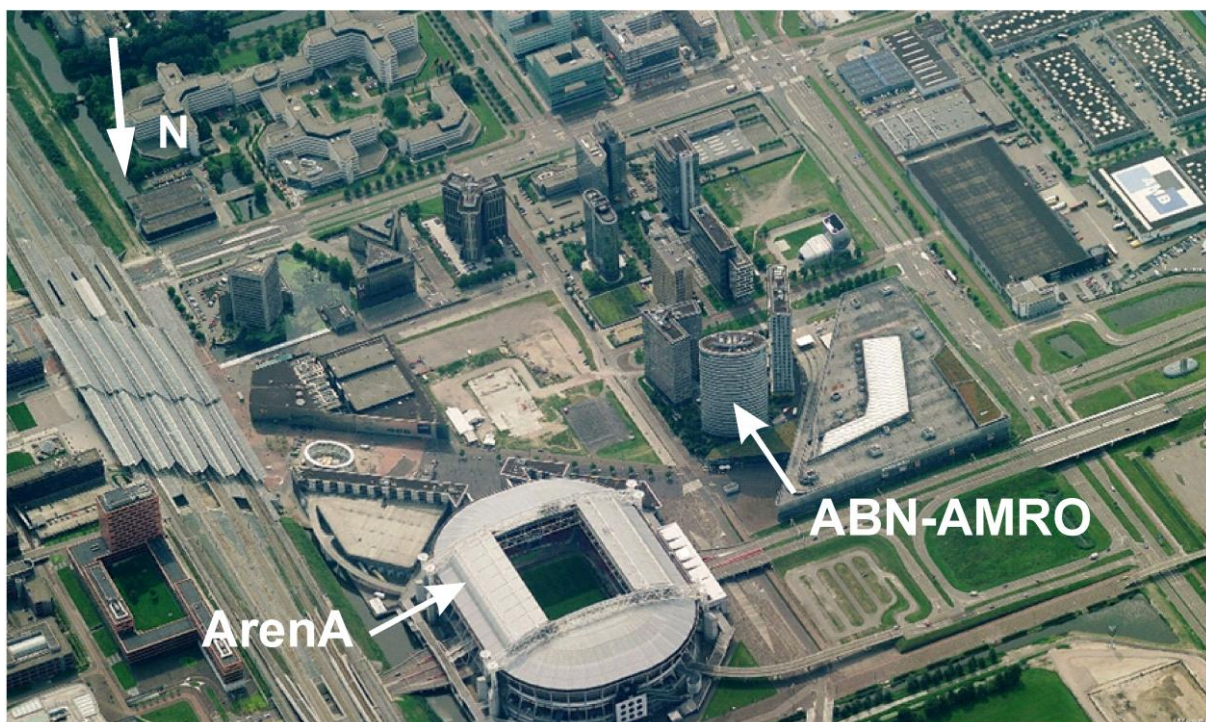


Fig. 1. Aerial view from north of Amsterdam Arena football stadium and surroundings. The ABN-AMRO tower is indicated.

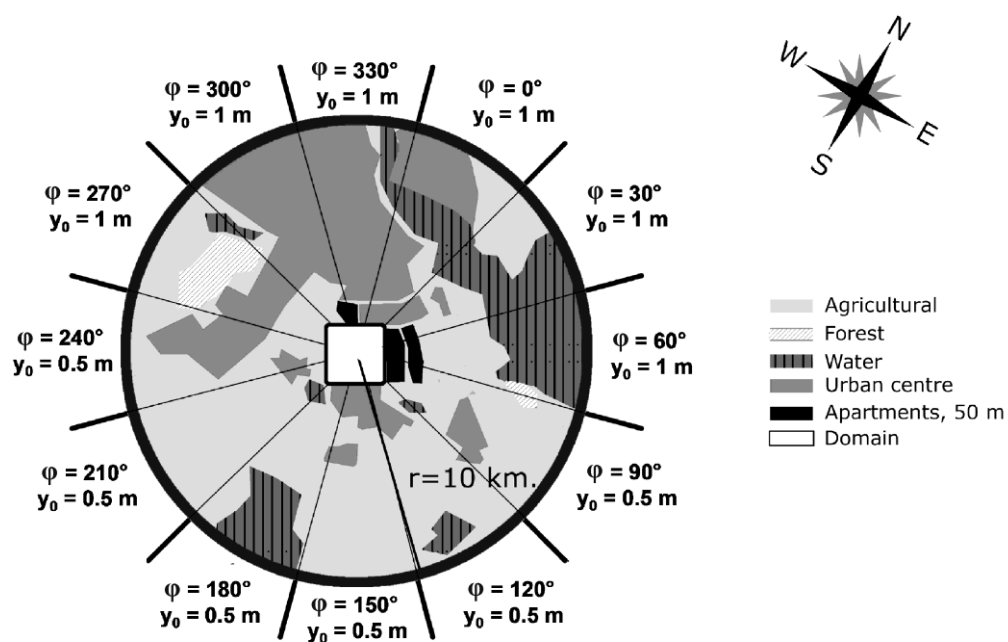


Fig. 2. Terrain surrounding the stadium with a radius of 10 km and estimated aerodynamic roughness length y_0 based on an upstream distance of 10 km. The white square represents the computational domain used in this study.

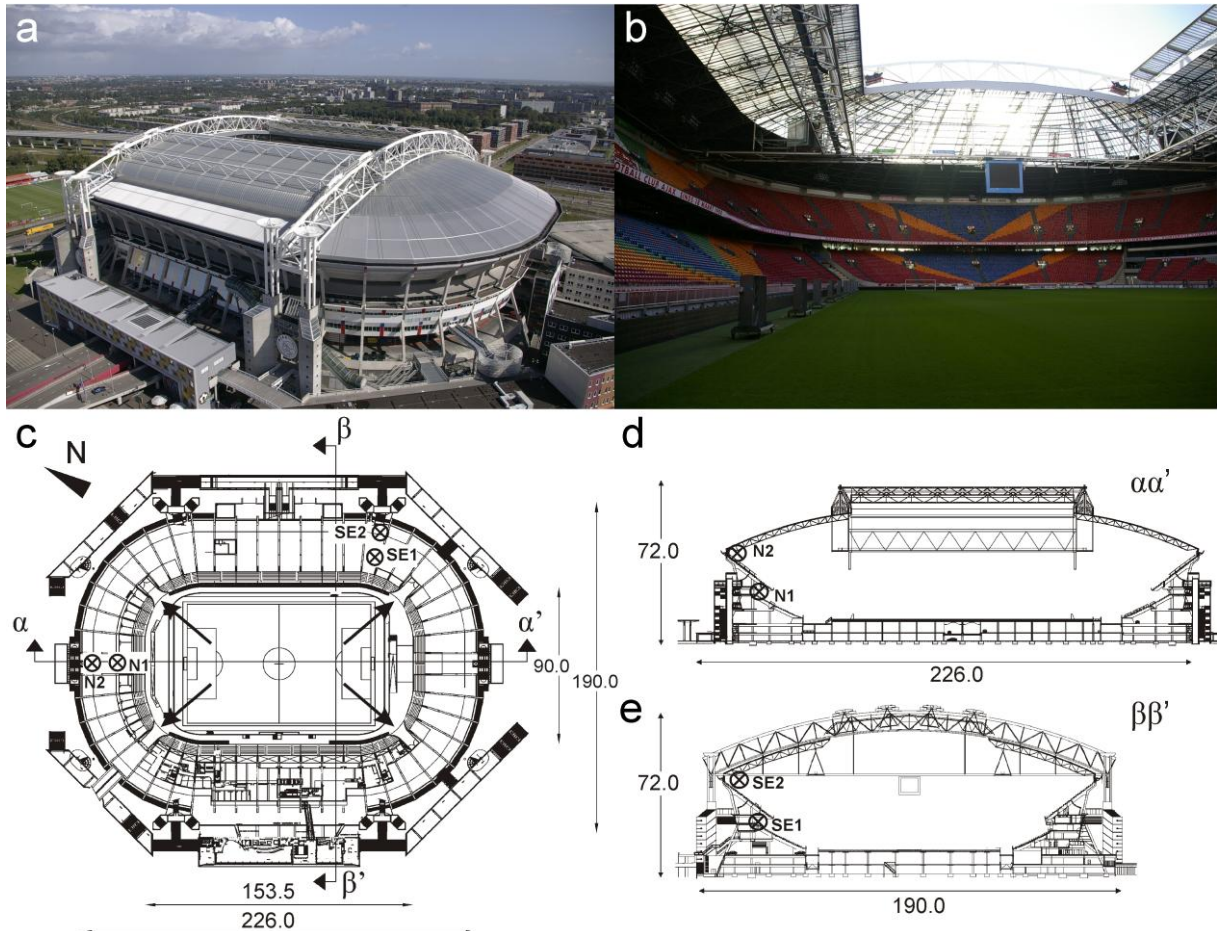


Fig. 3. Amsterdam ArenaA stadium. (a) Aerial view of the stadium with the roof opened; (b) stadium interior; roof is open; (c) horizontal cross-section at a height of 2 m above the deck, which is situated at 8.5 m above ground level. The four arrows indicate the location of the openings in the corners of the stadium (gates), (d) vertical cross-section $\alpha\alpha'$; (e) vertical cross-section $\beta\beta'$. The four measurement positions (\otimes) for air temperature and CO_2 concentration inside the stadium are indicated. Dimensions in m.

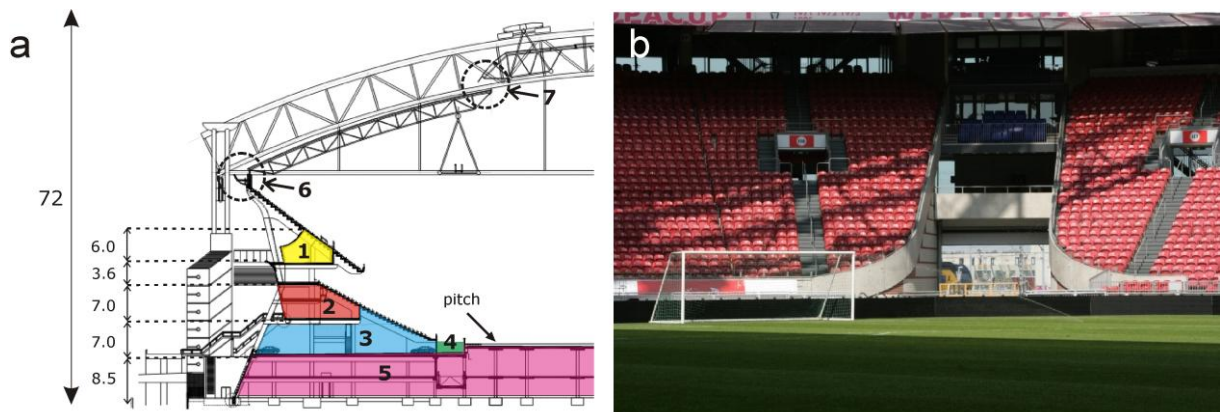


Fig. 4. (a) Vertical cross-section of the eastern part of the ArenaA. (1) logistics ring with entrances to the stands on the second tier; (2) logistics ring with entrances to the stands on the first tier; (3) the ArenaA deck that contains the gates; (4) safety and logistics ring between the stands and the pitch; (5) car park underneath the pitch; (6) ventilation opening between stand and steel roof construction; (7) ventilation opening between the fixed and movable part of the roof. Dimensions in m. (b) One of the four openings in the corner of the stadium (gates)

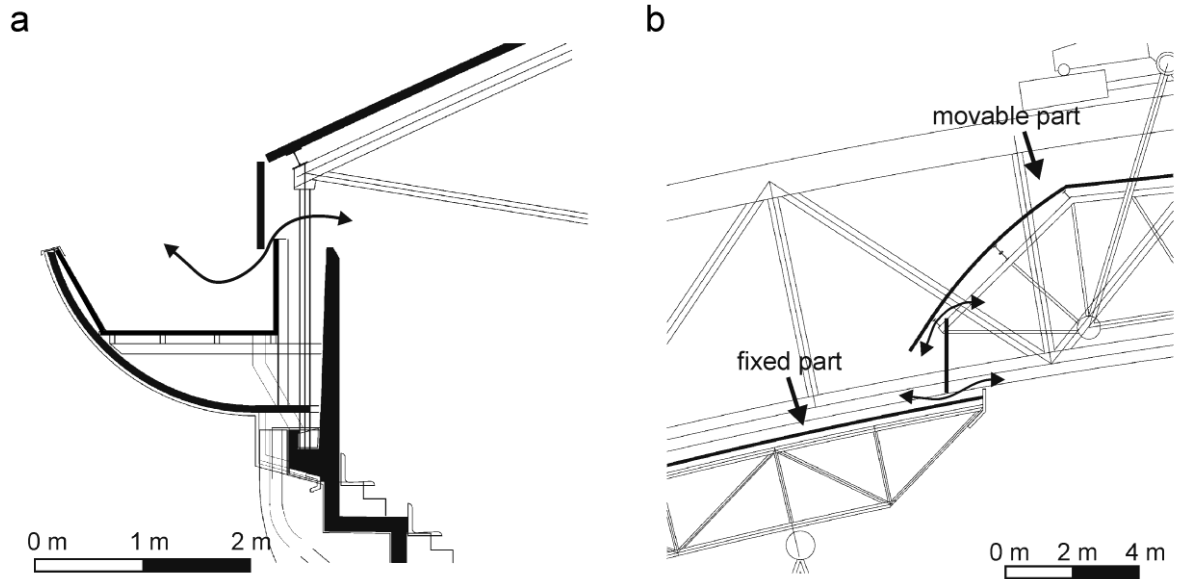


Fig. 5. Cross-sections of the ventilation openings in the upper part of the stadium; (a) ventilation opening between the steel roof construction, the gutter and the concrete stand, present along the entire perimeter of the stadium (see nr. 6 in Fig. 4a); (b) ventilation opening between the fixed and movable part of the roof. This opening is only present at the two longest edges of the stadium (see nr. 7 in Fig. 4a).

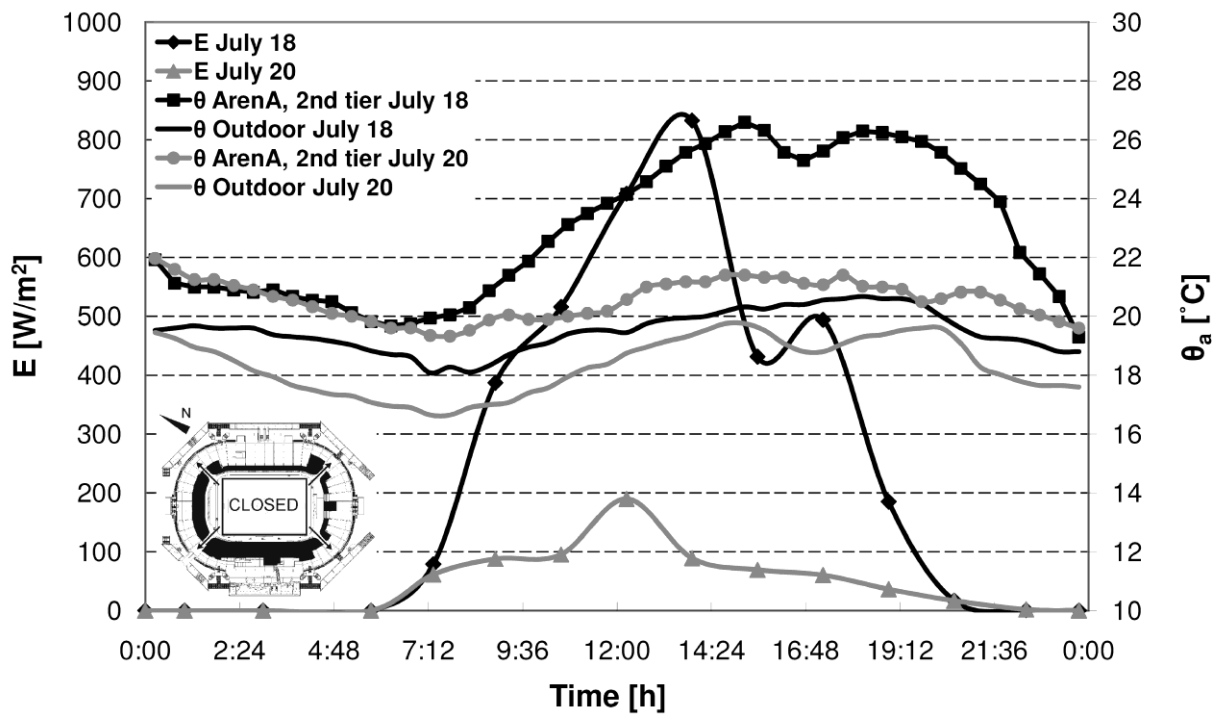


Fig. 6. The measured irradiance E and the measured air temperature θ_a inside and outside the stadium on a sunny day (July 18, 2007) and a cloudy day (July 20, 2007).

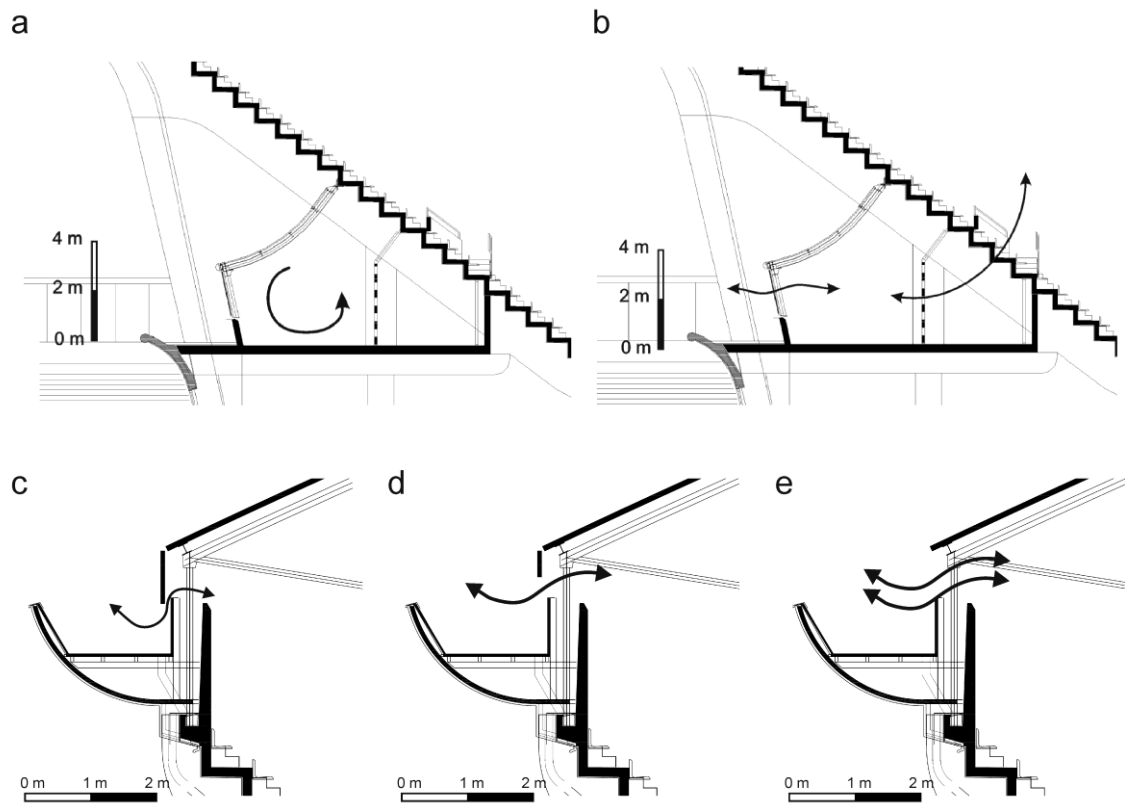
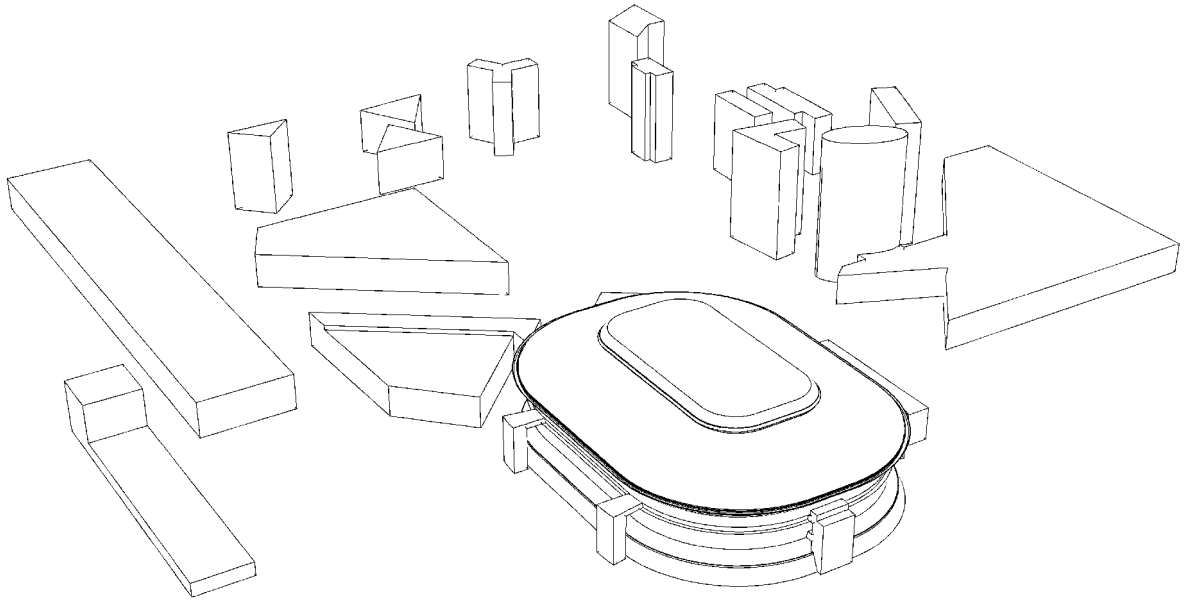


Fig. 7. Cross-sections of the logistics ring on the second tier (Fig. 4a; nr. 1) with (a) current ventilation configuration; (b) alternative ventilation configuration 1 in which eight windows are opened connecting the outdoor and indoor environment. (c-e) Cross-sections of the ventilation opening between the steel roof construction, the gutter and the concrete stand; (c) for current configuration; (d) for configuration 2 (half of the steel sheets removed); (e) for configuration 3 (steel sheets removed entirely).

a



b

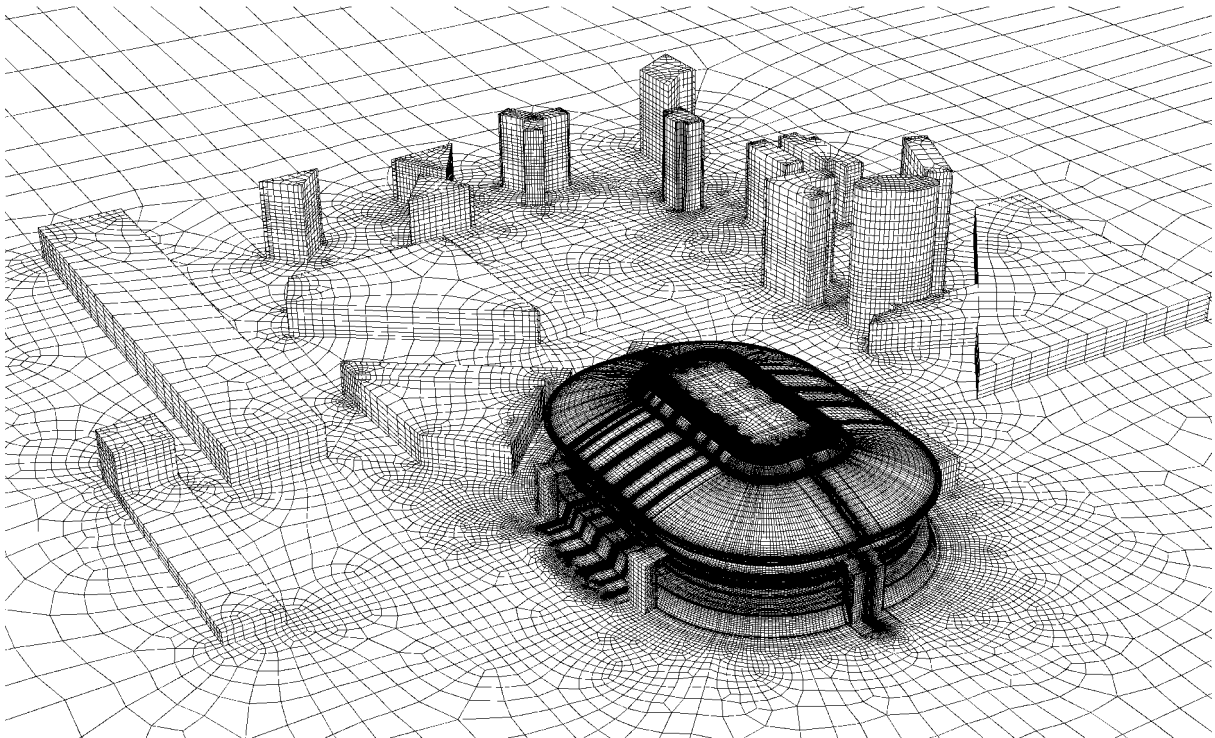


Fig. 8. (a) Computational model geometry, view from northeast; (b) Computational grid on the building surfaces and part of the ground surface. A high resolution is used in the proximity of the stadium, and a lower resolution at a larger distance from the stadium.

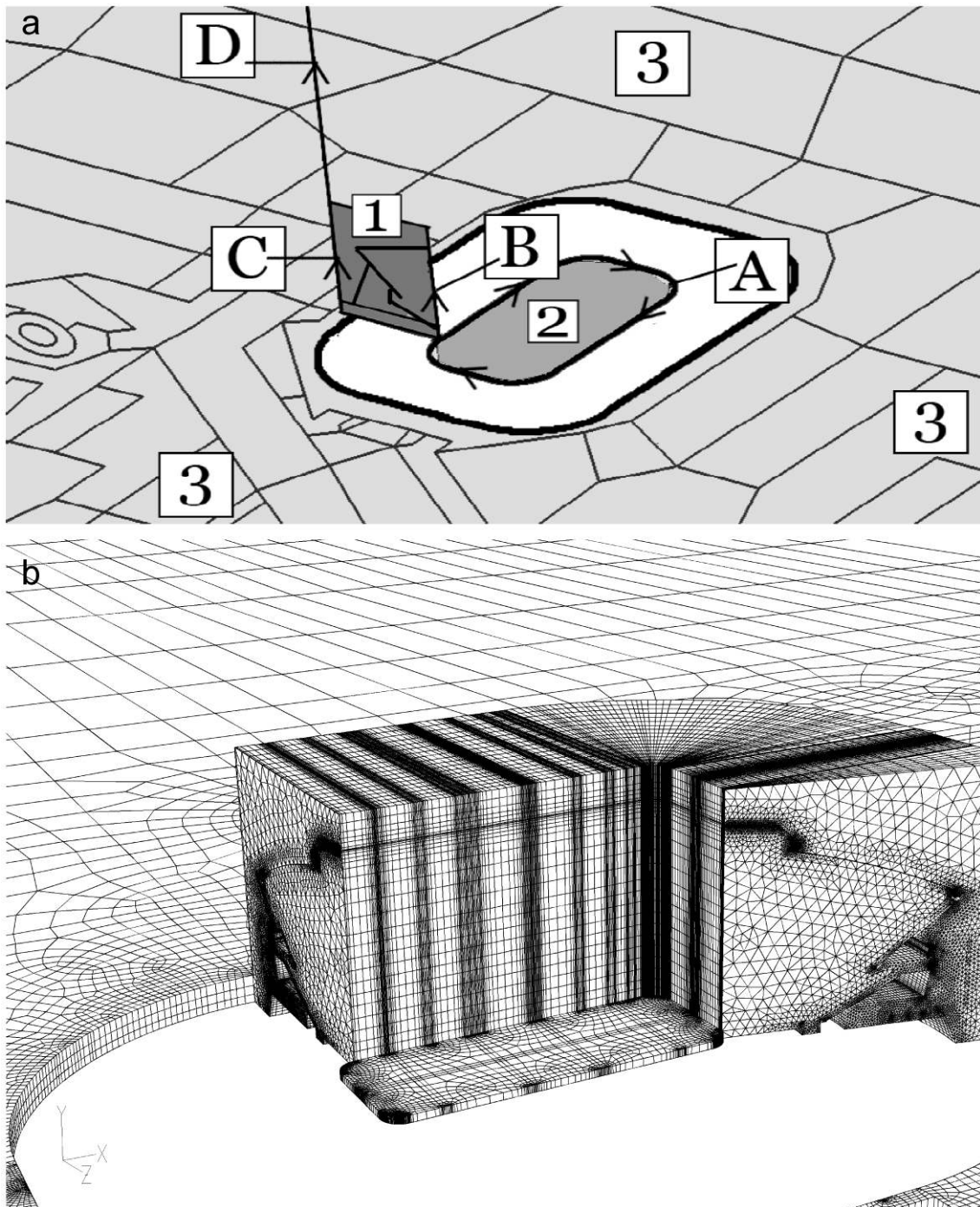


Fig. 9. (a) Schematic representation of the procedure for computational geometry and grid generation; (b) part of the grid illustrating some meshed cross-sections and resulting parts of the volume grid.

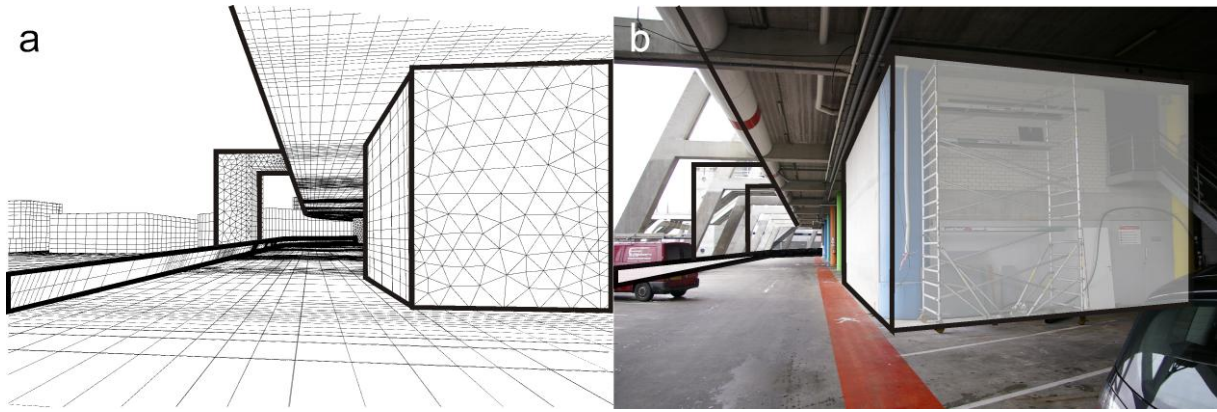


Fig. 10. (a) Detail of the computational grid on the east side of the stadium; (b) Corresponding picture taken at the east side of the stadium.

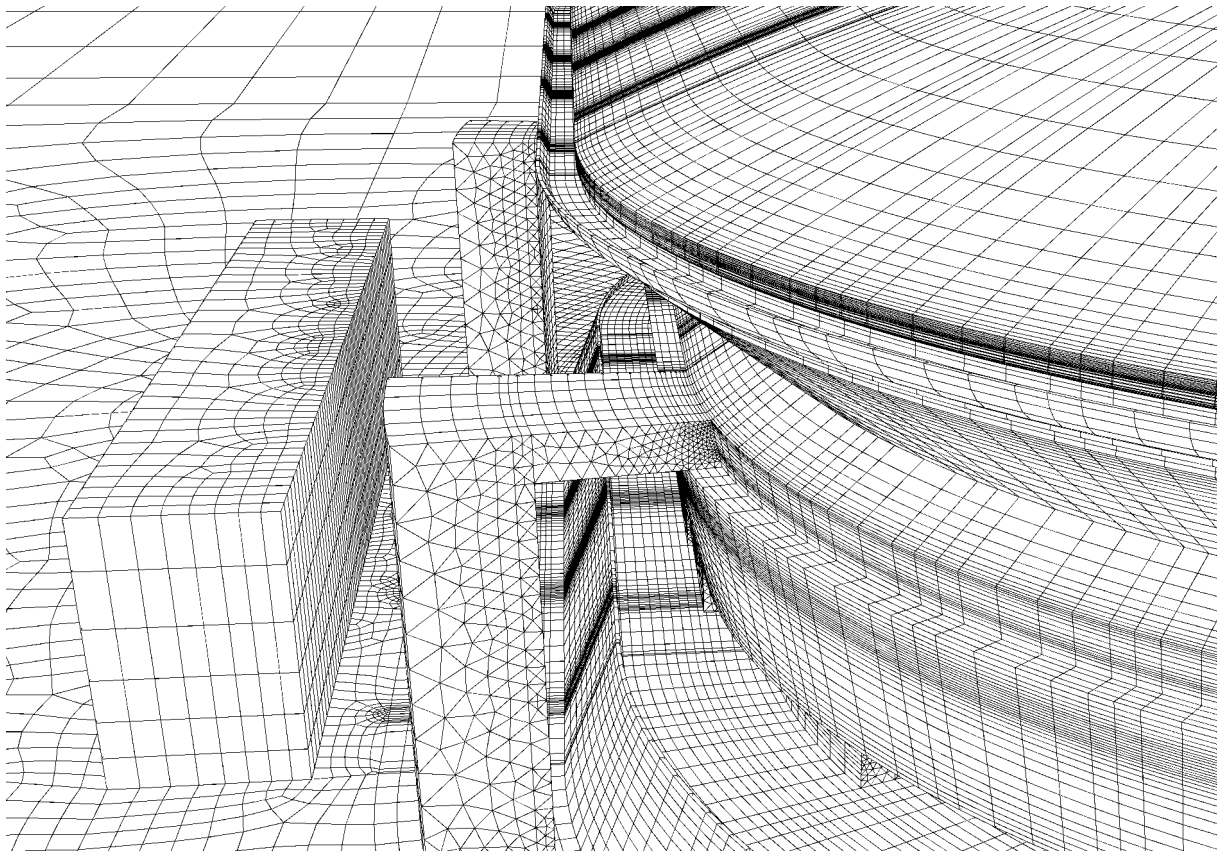


Fig. 11. Bird-eye view of the grid on the southeast side of the stadium, illustrating details such as the roof gutter which is modelled in detail for the air flow through the nearby ventilation opening (Fig. 5a).

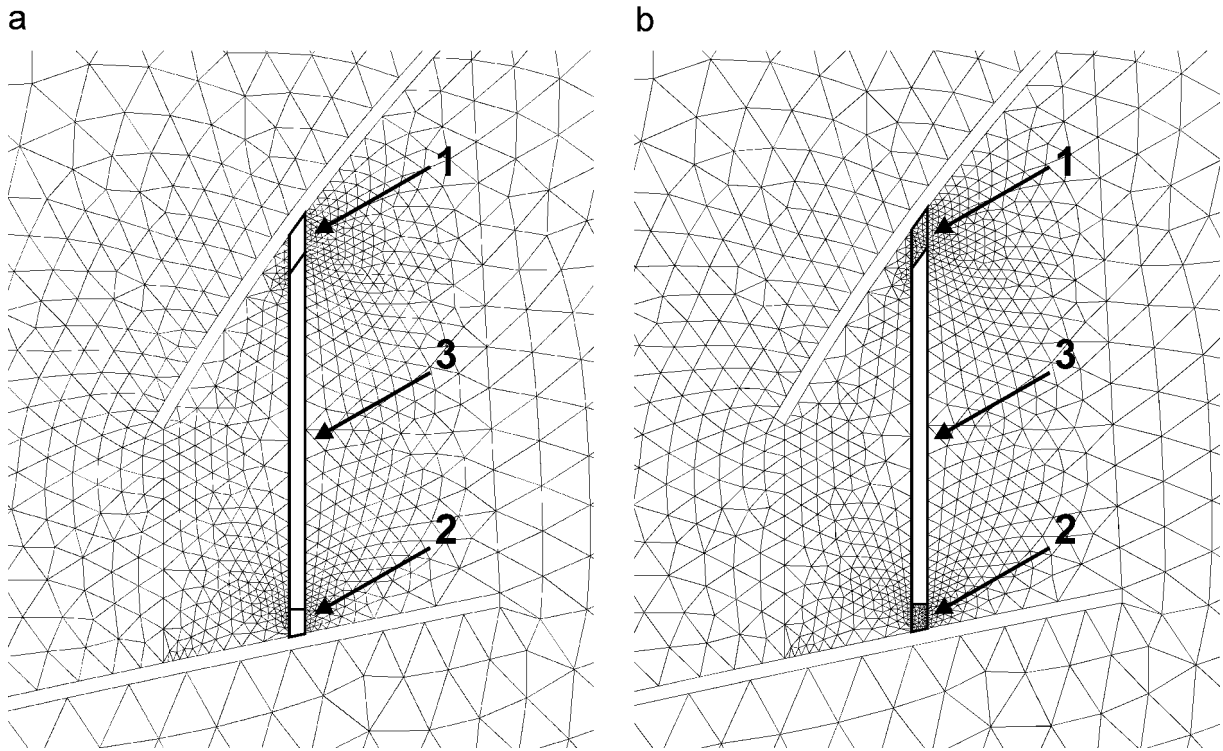


Fig. 12. Ventilation opening between the fixed and movable part of the roof (see Fig. 5b). Three meshed volumes (indicated by the bold lines and with numbers 1-3) have been implemented to generate different grids with small geometric changes: (a) All meshed volumes deleted; no opening present; (b) only meshed volume 3 deleted; small openings 1 and 2 present. Another option would be deleting none of the meshed volumes, in which case a large opening would be created.

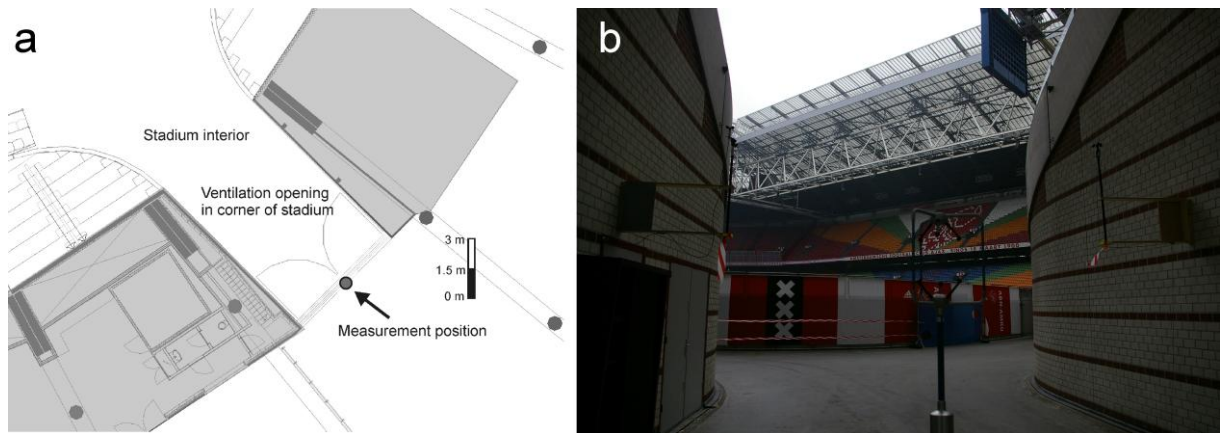


Fig. 13. Position of wind speed measurements with ultrasonic anemometers in the ventilation openings at the corners of the stadium (gates).

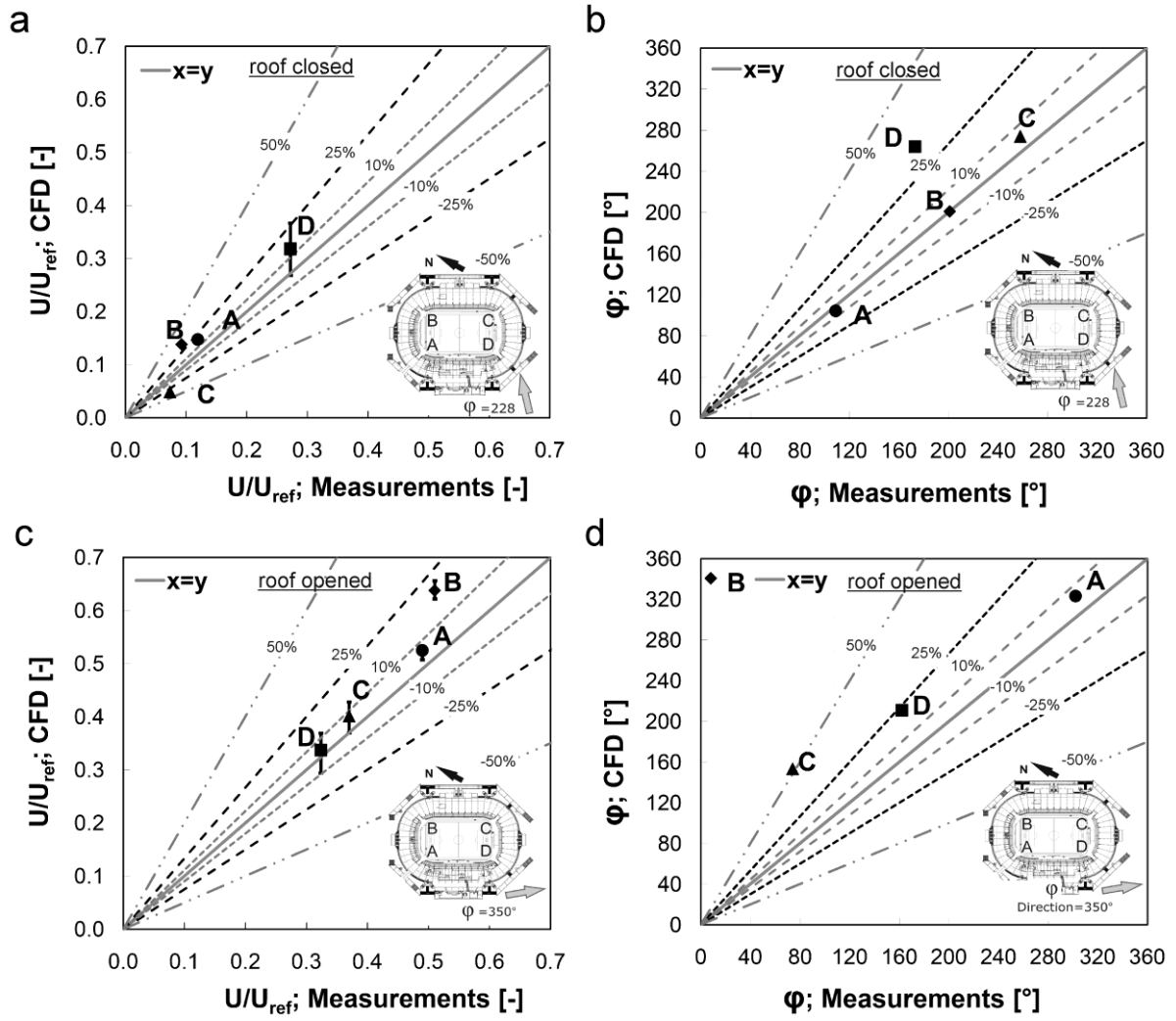
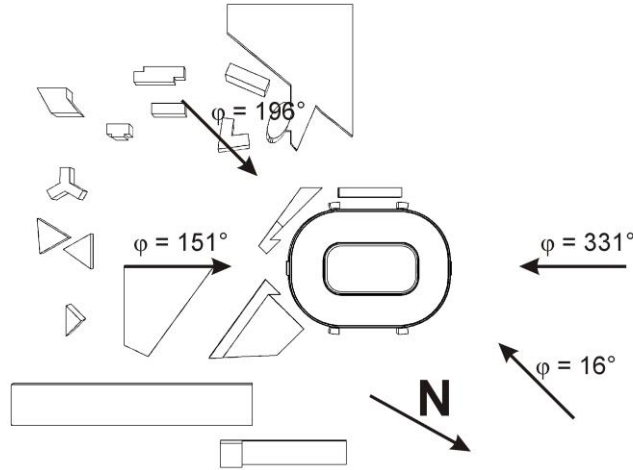
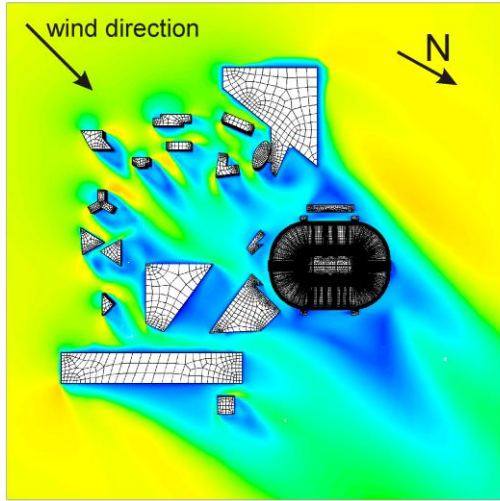


Fig. 14. (a-b) Comparison between numerical and experimental results in the four gates A, B, C and D, for closed roof and wind direction of 228° : (a) non-dimensional velocity magnitude U/U_{ref} ; (b) wind direction ϕ . (c-d) Same as (a-b), but for open roof and wind direction of 350° : (c) non-dimensional velocity magnitude U/U_{ref} ; (d) wind direction ϕ . The error bars are a measure of the local spatial gradients in the CFD simulation.

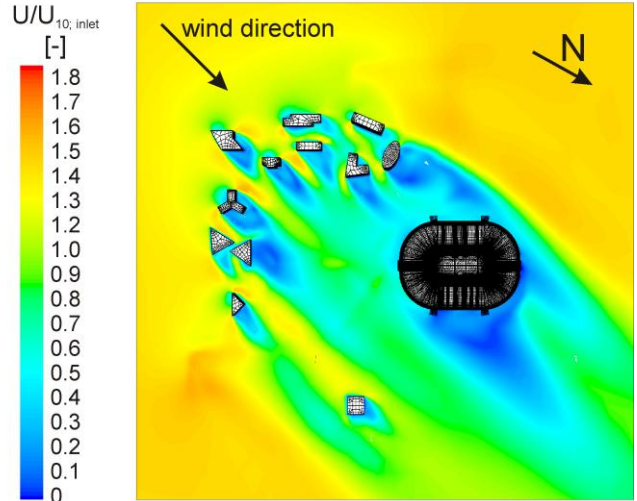
a



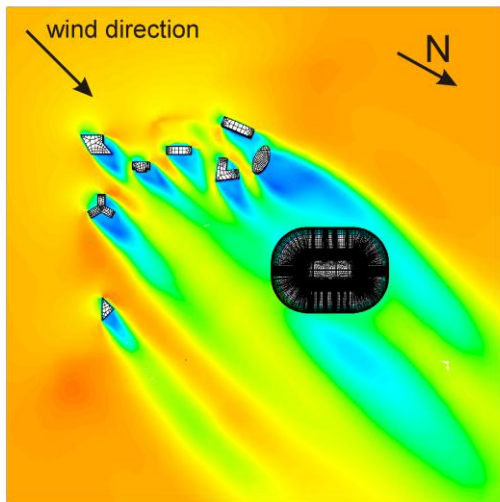
b



c



d



e

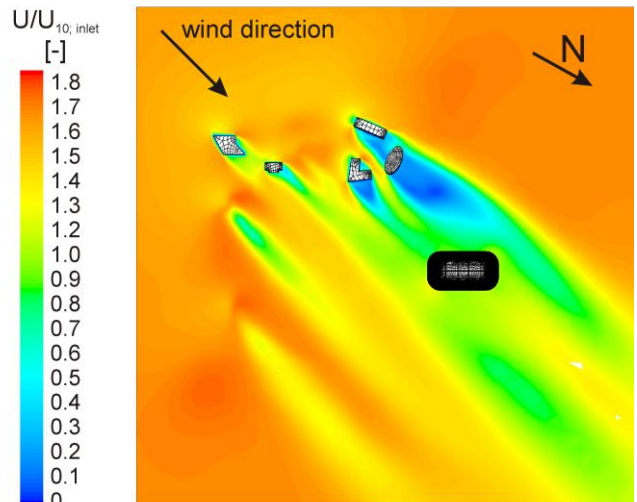


Fig. 15. (a) Top view of stadium and surrounding buildings with indication of wind directions for the CFD simulations ($\phi = 16^\circ$, 151° , 196° and 331°). (b-e) Contours of non-dimensional velocity magnitude U/U_{10} in four horizontal planes, for $\phi = 196^\circ$ (SSW) and $U_{10} = 5$ m/s; at (b) 10 m; (c) 20 m; (d) 40 m and (e) 60 m above the ArenA deck. The lower wind speed ratios around the stadium indicate that it is situated in the wake of the surrounding buildings, which causes the lower air exchange rates for this wind direction.

Tables

Table 1. Ventilation openings present in the stadium with their surface area (m²).

| Ventilation opening | Surface area (m ²) |
|---|--------------------------------|
| Roof | 4,400 |
| Four openings in corners of stadium (Fig. 3c, 4b) | 166 |
| Opening between stand and roof construction (Fig. 5a) | 130 |
| Opening between fixed roof and movable roof (Fig. 5b) | 85 |

Table 2. Calculated air change rate per hour (ACH) for the current situation and for four alternative ventilation configurations, for reference wind speed $U_{10} = 5$ m/s, for wind directions $\varphi = 16^\circ, 151^\circ, 196^\circ$ and 331° and for fixed indoor surface temperatures.

| Ventilation configuration | ACH (h^{-1}) | | | | |
|---------------------------|-------------------------|-------------|-------------|-------------|---------|
| | φ ($^\circ$) | | | | Average |
| | 16° | 151° | 196° | 331° | |
| Current situation | 1.51 | 1.33 | 1.11 | 1.49 | 1.36 |
| Configuration 1 | 1.56 | 1.52 | 1.12 | 1.33 | 1.38 |
| Configuration 2 | 1.91 | 1.61 | 1.29 | 1.54 | 1.59 |
| Configuration 3 | 2.19 | 2.28 | 1.61 | 1.72 | 1.95 |
| Configuration 4 | 4.57 | 3.40 | 2.66 | 3.41 | 3.51 |